



CHORUS

This is the accepted manuscript made available via CHORUS. The article has been published as:

Martensitic fcc-hcp transformation pathway in solid krypton and xenon and its effect on their equations of state

A. D. Rosa, A. Dewaele, G. Garbarino, V. Svitlyk, G. Morard, F. De Angelis, M. Krstulović, R. Briggs, T. Irifune, O. Mathon, and M. A. Bouhifd

Phys. Rev. B **105**, 144103 — Published 15 April 2022

DOI: [10.1103/PhysRevB.105.144103](https://doi.org/10.1103/PhysRevB.105.144103)

Martensitic fcc-hcp transformation pathway in solid krypton and xenon and its effect on their equation of states

A.D. Rosa^{1*}, A. Dewaele^{2,3}, G. Garbarino¹, V. Svitlyk¹, G. Morard⁴, F. De Angelis⁵, M. Krstulović⁶, R. Briggs⁷, T. Irifune⁸, O. Mathon¹ and M.A. Bouhifd⁹

^{1.} *European Synchrotron Radiation Facility (ESRF), 71, Avenue des Martyrs, Grenoble, France.*

^{2.} *CEA, DAM, DIF, 91297 Arpajon Cedex, France*

^{3.} *Université Paris-Saclay, CEA, Laboratoire Matière en Conditions Extrêmes, 91680 Bruyères-le-Châtel, France*

^{4.} *Université Grenoble Alpes, Université Savoie Mont Blanc, CNRS, IRD, IFSTTAR, ISTerre, 38000 Grenoble, France*

^{5.} *Dipartimento di Fisica, Università di Roma La Sapienza - Piazzale Aldo Moro 5, 00185 Roma, Italy*

^{6.} *University of Potsdam, Institute of Geosciences, Karl-Liebknecht-Str. 24-25, 14476 Potsdam-Golm, Germany*

^{7.} *Lawrence Livermore National Laboratory, Livermore, CA, United States of America*

^{8.} *Geodynamics Research Center, Ehime University, 2-5 Bunkyo-cho, Matsuyama 790-8577, Japan*

^{9.} *Laboratoire Magmas et Volcans, Université Clermont Auvergne, CNRS, IRD, OPGC, F-63000 Clermont-Ferrand, France*

*corresponding author: angelika.rosa@esrf.fr

21 **Abstract**

22 The martensitic transformation is a fundamental physical phenomenon at the origin of
23 important industrial applications. However, the underlying microscopic mechanism, which is of
24 critical importance to explain the outstanding mechanical properties of martensitic materials, is
25 still not fully understood. This is because for most martensitic materials the transformation is a
26 fast process that makes *in situ* studies extremely challenging. Noble solids krypton and xenon
27 undergo a progressive pressure induced fcc to hcp martensitic transition with a very wide
28 coexistence domain. Here, we took advantage of this unique feature to study the detailed
29 transformation progress at the atomic level by employing *in situ* X-ray diffraction and absorption
30 spectroscopy. We evidenced a four stages pathway and suggest that the lattice mismatch between
31 the fcc and hcp forms plays a key role in the generation of strain. We also determined precisely
32 the effect of the transformation on the compression behavior of these materials.

33 **1. Introduction**

34 Martensitic phase transitions are fundamental first-order transformations that are, for
35 instance, at the origin of steel hardening and shape memory effects (see [1] for review). They are
36 diffusionless and proceed through the collective displacement of neighboring atoms. These subtle
37 local atomic movements are at the origin of drastic changes in the materials' mechanical [2-4],
38 transport [5] and electromagnetic [6] properties. Such transformations have been described in
39 various materials such as pure metals and binary alloys [1,7-20], semiconductors [21], Zr-based
40 ceramics [22] and proteins [23] that are important for the high-tech industry, planetary and life
41 sciences. In the past decades, significant research efforts have been invested to explore the
42 microscopic origin of martensitic transformations, but the exact transformation pathway and

43 microstructural evolution is still debated. This lies in the very rapid nature of the first-order
44 transformation that makes the monitoring of the phase transformation progress and mechanism
45 extremely challenging. For this reason, most of the experimental investigations of the
46 microstructural evolution of martensitic materials were conducted *ex situ* using a variety of
47 techniques such as optical microscopy, scanning electron microscopy, transmission electron
48 microscopy (TEM) and X-ray diffraction [18-20], performed on (partially) transformed systems.
49 However, a major obstacle lies in the capacity of such techniques to disentangle the different
50 effects occurring during the fast phase transition when it proceeds. In particular, they do not give
51 access to the variation of the atomic distances of the parent and martensitic phase during the
52 transformation at the relevant conditions that may play a key role in the building-up and
53 accumulation of strain in the material structure. Few *in situ* studies have been performed including
54 neutron and X-ray diffraction or TEM [24-27] but would require higher time resolution to capture
55 the different steps of the transformation. Only few recent studies reported the potential of proxy
56 systems such as colloidal crystals to reveal kinetic features of martensitic transformations [28].

57 The heavy noble gas solids xenon (Xe) and krypton (Kr) undergo a pressure induced phase
58 transition, from a face-centered cubic (fcc) to an hexagonal close packed (hcp) structure [29-32].
59 This transition exhibits fundamental similarities with the general features of martensitic fcc-hcp or
60 hcp-fcc transformations observed in metals and their alloys [7,9-16] that were first described by
61 Burgers for Zr [7]. These studies also evidenced the existence of a wide coexistence domain
62 between a face-centered cubic (fcc) and an hexagonal close packed (hcp) structure. In xenon, it
63 was shown that the completion of the transformation occurs at 65 GPa and the extent of the
64 coexistence domain is not affected by temperature annealing [30,31]. As recently reported in [32],
65 a similar behaviour was observed in solid krypton but with a much wider coexistence domain of

66 ~400 GPa. Here again, the transition is not affected by temperature annealing attesting that it is
67 not kinetically hindered [32]. The existence of such a large coexistence domain has been associated
68 to the proximity of the Gibbs free energies of the fcc and hcp forms [29,33,34], which is another
69 fundamental feature of martensitic transformations. The progressive pressure induced fcc-hcp
70 transition in NGs could represent a model system to interpret such transitions in more complex
71 materials at the microscopic level.

72 The main objective of this experimental study is to exploit the progressive nature of the
73 fcc to hcp conversion in solid Xe and Kr to *in situ* capture and characterize the different stages of
74 the martensitic transformation. To this aim, we combined two complementary *in situ* probe
75 techniques: X-ray diffraction (XRD) and absorption spectroscopy (XAS) that provide insights into
76 the atomic arrangement at the bulk and local scales, respectively. We also aimed at determining
77 the effect of this transformation on the mechanical properties of the pure and mixed fcc-hcp phases
78 for xenon and krypton.

79 **2. Methods**

80 All the experimental work was carried out at the X-ray absorption and X-ray diffraction
81 beamlines ID24, BM23 and ID27 at the European Synchrotron Radiation Facility (ESRF) [35-37].
82 These three beamlines are optimal for performing very high-pressure experiments as they provide
83 very intense, highly focused, high-energy X-ray beams. A list of the experimental conditions is
84 presented in **Table I** of the main text.

85 **2.1 XRD data acquisition and analysis**

86 At the beamline ID27, monochromatic X-rays with wavelength $\lambda=0.3738 \text{ \AA}$ were selected
87 using a silicon (111) channel-cut monochromator and focused down to $3 \times 3 \text{ \mu m}^2$ (FWHM) using a

88 pair of Kirkpatrick-Baez (KB) mirrors [37]. The X-ray diffraction data were collected on a
89 MAR165 planar CCD detector. A high purity cerium oxide powder was used as standard to
90 accurately determine the integration parameters (detector tilt angles, sample to detector distance,
91 detector beam center and instrumental peak broadening). Two kinds of diffraction images were
92 acquired including continuous oscillation images over omega (Ω) range of $\pm 30^\circ$ and step-
93 oscillations images over the same Ω range using an Ω step size of 1° . The software CrysAlisPro
94 was used to analyze the step-scan oscillation images [38] for the low pressure points. The software
95 Fit2D [39] was used to generate slices of 1-dimensional diffraction patterns along the azimuth for
96 further Rietveld refinement of textured samples (2θ range up to 17°). The software MAUD [40]
97 was employed to extract the unit cell volumes, volume fractions and coherently diffracting domain
98 sizes (**Fig. S1** of the **Supplementary Material** [41]) .

99 Two independent XRD runs referred to as run-1 and run-2 were carried out at the beamline
100 ID27 (**Table I**). High purity xenon (99.999%) from the company Messer France was loaded in
101 membrane diamond anvil cells (DACs) equipped with single-crystal diamonds of 150 μm and 300
102 μm culet size, respectively. A hole was drilled by laser machining on pre-indented rhenium gasket
103 to serve as a pressure chamber. Prior to the xenon gas loading a ruby sphere ($\sim 3 \mu\text{m}$ in diameter),
104 a 5 μm thick nickel foil and compressed gold powder pellet were placed in the pressure cavity. No
105 additional pressure-transmitting medium such as He or Ne gas was added to the sample to avoid
106 forming noble gas mixtures [42]. The pressure was measured using the standard ruby luminescence
107 technique using the calibration of Dewaele et., [43] and cross-checked using the unit-cell volume
108 variation of nickel and gold using their well-established equation of states [43]. Nickel was only
109 used as pressure calibrant at room temperature and prior to any laser annealing as it was shown
110 that, in presence of noble gases, its compressional behaviour is substantially affected by high

111 temperature treatment as noble gases can get incorporated in transition metals [32,44,45]. This
 112 material was also employed as YAG laser radiation absorber to evaluate the effect temperature
 113 annealing on the fcc-hcp transition in xenon. The annealing temperature was measured by
 114 analyzing the thermal emission as described in reference [46]. Deviatoric or non-hydrostatic
 115 stresses in the sample chamber were monitored using the analysis of the XRD peak positions of
 116 gold following well established protocols [47]. For clarity, considering the large amount of
 117 collected XRD data points (> 100), we have reported the pressure-volume (P - V) data in **Table SI**
 118 of the **Supplementary Material**.

119 **Table I.** List of the experimental conditions. BL: beamline, SC: single crystal, NPD: nano-
 120 polycrystalline diamond. Raw data are presented in **Fig. S1-3**.

Element	run number	BL	technique	beam size (μm^2)	beam energy (keV)	pressure range (GPa)	pressure standard	diamond type
Xenon	1	ID27	XRD	3x3	33.17	0-86	Au, Ni, ruby	SC
	2							
	3	BM23	EXAFS	5x5	34.56	0-155	ruby, Re	NPD
Krypton	5	ID24	EXAFS	10x10	14.33	15-68	ruby	NPD
	6							

121

122 2.2 XAS data acquisition and analysis

123 The evolution of the local atomic arrangements of xenon and krypton with pressure were
 124 investigated at the two X-ray absorption (XAS) beamlines BM23 and ID24, respectively. BM23
 125 is the only ESRF beamline that enables micro-XAS acquisitions at X-ray energies higher than 20
 126 keV [36]. This instrument is well suited for XAS studies in a DAC at the high energy K-edge of

127 xenon (34.56 keV). It is equipped with a high-resolution Si(311) double-crystal monochromator
128 and a Pt-coated KB-mirror system for X-ray beam focusing down to $5 \times 5 \mu\text{m}^2$ (FWHM) and higher
129 harmonics rejection. Two ion chambers were used to measure the incident (I_0) and transmitted (I_t)
130 intensities filled with appropriate gas mixtures of krypton and helium to achieve signal absorption
131 of 30% and 70%, respectively. The local structure of krypton (K-edge energy of 14.385 keV) was
132 investigated at the energy-dispersive XAS beamline ID24 [35]. At this instrument, a high intensity
133 and highly focused X-ray beam of $10 \times 10 \mu\text{m}^2$ (FWHM) is generated by a Si(111) polychromator
134 and rhodium-coated mirrors. The incident and transmitted intensities were recorded using a
135 FReLoN CCD camera as described in Rosa et al. [32].

136 Three independent XAS runs referred to as run-3, run-4 and run-5 were performed (**Table**
137 **I**). Run-3 was devoted to xenon and performed at BM23 while run-4 and -5 were focused on
138 krypton and carried out at ID24 (examples of raw data are presented in **Fig. S2** and **Fig. S3** of the
139 **Supplementary Material**). Typical data acquisition times were 30 minutes and 50 milliseconds
140 at BM23 and ID24, respectively. For these runs all the DACs were equipped with nano-
141 polycrystalline diamonds that enable acquiring glitch-free, high quality EXAFS data [48]. As for
142 the experiments at ID27, a laser-drilled hole on a pre-indented rhenium gasket was employed as
143 pressure chamber. The high purity noble gases were loaded together with a small ruby sphere used
144 for pressure measurements following a similar procedure as described above. In run-3, at pressures
145 higher than 90 GPa, the pressure was determined by XRD using the unit-cell volume variation of
146 the rhenium gasket [49]. Diffraction data were collected at two distinct positions in the DAC to
147 evaluate the pressure gradient across the sample. For these measurements, a MAR165 diffraction
148 detector was installed at BM23 at a distance of 197.37 mm from the sample and XRD images were

149 acquired without oscillation at a wavelength of 0.3594 Å (34.5 keV). The dimensions of the
150 diamond culets and the investigated pressure domains for the different runs are listed in **Table I**.

151 For both xenon and krypton, we used a similar data reduction procedure to determine the
152 local lattice distortion in the first stacking layer and, to follow qualitatively the evolution of
153 potential lattice distortions up to the third stacking layer (**Fig. 1**). EXAFS spectra were normalized,
154 converted from energy to k -space $\chi(k)$ and Fourier-transformed using a Kaiser-Bessel envelop and
155 further analyzed without phase-shift using the ARTEMIS software package [50].

156 EXAFS is sensitive to local distortions including coexisting domains, stacking faults and
157 grain-boundaries, which cannot be easily quantified by XRD. The focus of the present EXAFS
158 analysis resided on the identification of the extend of such local structural distortions in the bulk
159 sample. We aimed at monitoring the growth of hcp stacking faults having smaller lattice volumes
160 than the host fcc phase as seen using XRD in Kr by Rosa et al. [32].

161 The signal obtained in transmission XAS geometry represents the average of atomic
162 environments probed around an absorbing atom. Therefore, the signal contains contributions from
163 atoms in fcc and hcp structural environments. The signal contribution of each phase is linearly
164 dependent on its volumetric fraction in the present case. The most intense signals of both forms,
165 fcc and hcp, emerges from scattering of the first and second stacking layers (**Fig. 1**). In these
166 environments, an atom exhibits an equivalent number of next-nearest neighbors (N_1 and N_2) and,
167 also similar interatomic distances (R_1 and R_2) if the two forms have the same unit cell volumes.
168 Beyond the third stacking layer the scattering signals are different in the two phases, that exhibit
169 either a ABCABC stacking sequence (fcc) or a ABABAB stacking sequence (hcp) (**Fig. 1**, R3 and
170 R5). Because of the similarities of the scattering signals for the hcp and fcc phases in the most
171 intense part of the signal and the expected low lattice volume difference of only 4% between fcc

172 and hcp forms [32], we did not intend to extract individual lattice volumes and volumetric fractions
173 for the coexisting phases from the EXAFS data. The contributions of the coexisting forms could
174 only be resolved at higher signal frequencies that exhibit low amplitudes (**Fig. 1**). The refinement
175 of the volume fractions for the two coexisting structures would have therefore increased the
176 number of fitted variables beyond the number of independent points.

177 The present EXAFS analysis mainly aimed at extracting the average atomic distances for
178 the next nearest neighbor R_I which emerges from the scattering contribution of the coexisting fcc
179 and hcp forms, and the variation of R_I (σ_I) across the compressional anomaly. The volumetric
180 growth of dense hcp stacking faults would reduce the average next-nearest neighbor distances R_I
181 seen from XAS compared to the equilibrium distance R_0 observed for the bulk parent fcc phase
182 using XRD. In previous studies the observed differences between R_I and R_0 values from XAS and
183 XRD were assigned to the presence of significant atomic vibrational anisotropies that result
184 systematically in higher R_I values compared to R_0 (e.g. [51]). This work is focused on the relative
185 and not the absolute pressure induced changes of interatomic distances near the observed
186 compression anomaly to test the hypothesis if dense hcp stacking faults form in this pressure
187 interval.

188 In the present EXAFS analysis, all fittings were performed using a single structural input
189 model (fcc or hcp). To verify the robustness and independence of results for the first two scattering
190 paths, two adjustments were carried out for several EXAFS spectra, with the fcc and hcp models,
191 respectively. For each EXAFS fitting, the structural input models were calculated using the
192 equation of states of fcc and hcp Kr and Xe obtained from XRD. Theoretical backscattering
193 amplitudes and phase shift functions for fcc and hcp phases were computed subsequently using
194 the FEFF *ab initio* code included in ARTEMIS. The adjustments included a minimum of 2 and

195 up to 8 scattering paths similar to those employed by Filipponi and DiCicco [52]. The 8 scattering
196 paths included four single scattering paths up to the 5th shell excluding the direct 4th shell scattering
197 path due to its low probability (**Fig. 1**); four multiple-scattering paths that have an important
198 contribution to the EXAFS function such as the acute triangle in the first shell, the obtuse triangle
199 including atoms in the third shell; one forward and one double forward scattering path to atoms of
200 the 4th shell. For each scattering path the inter-atomic distance (R_i) and its distribution (σ_i^2) were
201 adjusted.

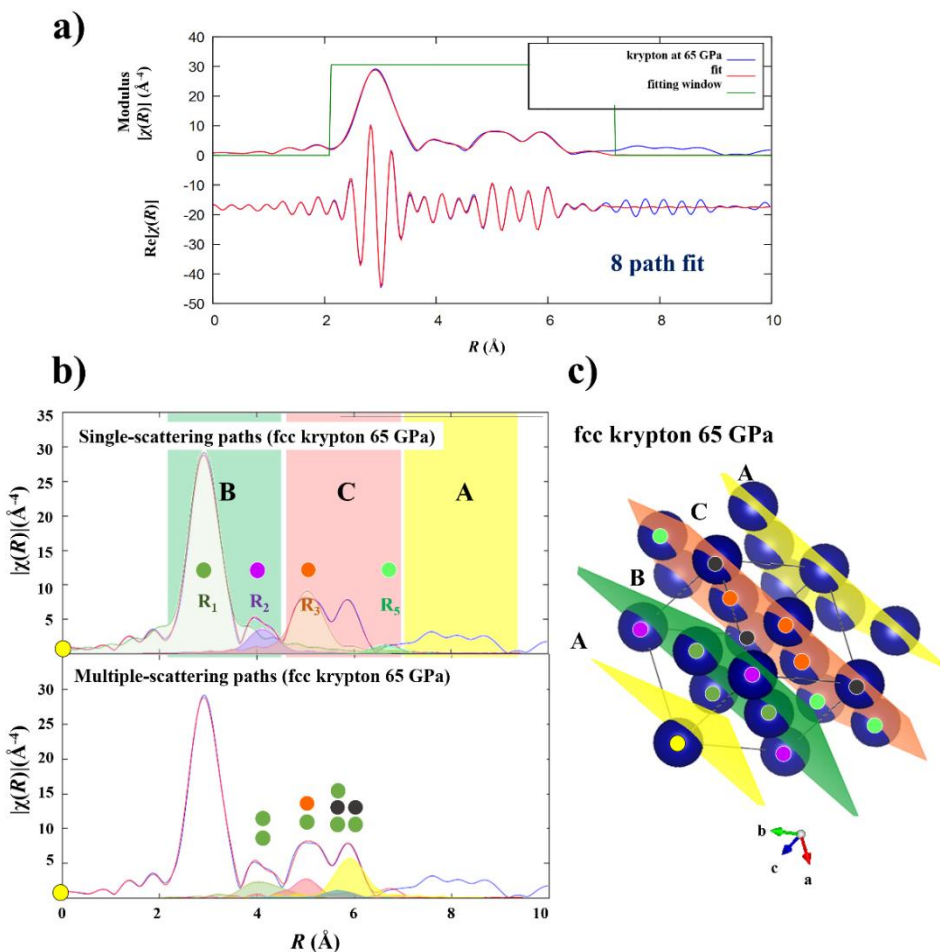
202 For xenon, we obtained lower EXAFS data quality at pressures below 10 GPa. In this case,
203 the adjustment window was shorter than the one employed for spectra obtained at higher pressure.
204 The Xe EXAFS functions were adjusted in the k -range between 3 to 9 \AA^{-1} (fitting window set
205 between 2 and 5.7 \AA) at pressures below 10 GPa and up to 14 \AA^{-1} (fitting window set between 2
206 and 8.5 \AA) beyond this pressure. Xe EXAFS data taken at the lowest pressure (5.9 and 8.5 GPa)
207 were fitted using an fcc structural model that contained 20 independent points and 15 adjusted
208 parameters including 7 structural parameters from 2 paths (R_1 and R_2) with each individually fitted
209 parameters R and σ^2 , the energy shift ΔE and 8 background parameters. At higher pressures
210 between 15 and 53.1 GPa, in the coexistence domain of the fcc and hcp forms, the Xe EXAFS
211 fittings were performed either with the fcc or hcp structural input model. Above 53.1 GPa and up
212 to 158 GPa, only the hcp structural input model was used. Both adjustments using the fcc or hcp
213 structural model contained up to 60 independent points and 33 adjusted parameters including 17
214 structural parameters from 8 paths with each individually fitted parameters R and σ^2 , the energy
215 shift ΔE and 16 fitted background parameters.

216 All Kr EXAFS functions were fitted using the fcc structural input model due to the low
217 volume fraction of the hcp phase (< 20%) in the investigated pressure range. The fitted k -range

218 was set from 3 to 10.5 \AA^{-1} (fitting window from 2 to 8 \AA). All fits were performed with k -weighting
 219 of 1, 2, and 3 and background adjustments to diminish correlations between σ^2 , R and ΔE_0 .

220 The results are listed in **Table SII** and **Table SIII**. The relative uncertainty on the first-
 221 neighbour distances (R_1) is smaller than ($5 \cdot 10^{-3}$) over the entire pressure range. The error on the
 222 extracted bond distance variation are in the order of 3%. Variations of ΔE may arise from the
 223 growing hcp phase that modifies the white line as shown in [32] for krypton. The R -factor is listed
 224 for each fit and presents a measure of the misfit between the raw data and the adjusted spectrum
 225 in % (a R -factor of 0.02 indicates a 2% misfit to raw data).

226



227

228 **Figure 1a) top panel:** Modulus of the krypton K-edge EXAFS function collected at 65 GPa representing
229 the distribution of average inter-atomic distances (R) seen from a central absorbing atom. The modulus is
230 obtained by Fourier transform of the normalized K-edge EXAFS functions (**Figures S2 and S3,**
231 **Supplementary Material**) after their conversion from energy to k -space and multiplication by k^2 ($k^3(\chi(k))$).
232 The amplitude of different peaks is proportional to the scattering probability. The blue lines represent the
233 modulus (top) and the real part (bottom) of the original data, the green line represents the fitting window
234 for the EXAFS analysis (phase shifted). The red lines represent the adjusted EXAFS spectrum. **b) bottom**
235 **panel:** Modulus of the EXAFS function as above (blue line) plotted together with the moduli of the 4 most
236 probable single-scattering paths (top) and the 4 most probable multiple-scattering paths (bottom) adjusted
237 in the fit. **c)** For clarity, a section of a fcc structure with the stacking sequence ABCA is shown on the right.
238 Atoms involved in the scattering paths emerging from the central atom (marked with a yellow circle) are
239 highlighted with circles of different color, corresponding to symbols and inter-atomic distances as marked
240 in the EXAFS modulus plots in **b)** on the left.

241

242 **3. Results and discussion**

243 **3.1 X-ray diffraction study of xenon**

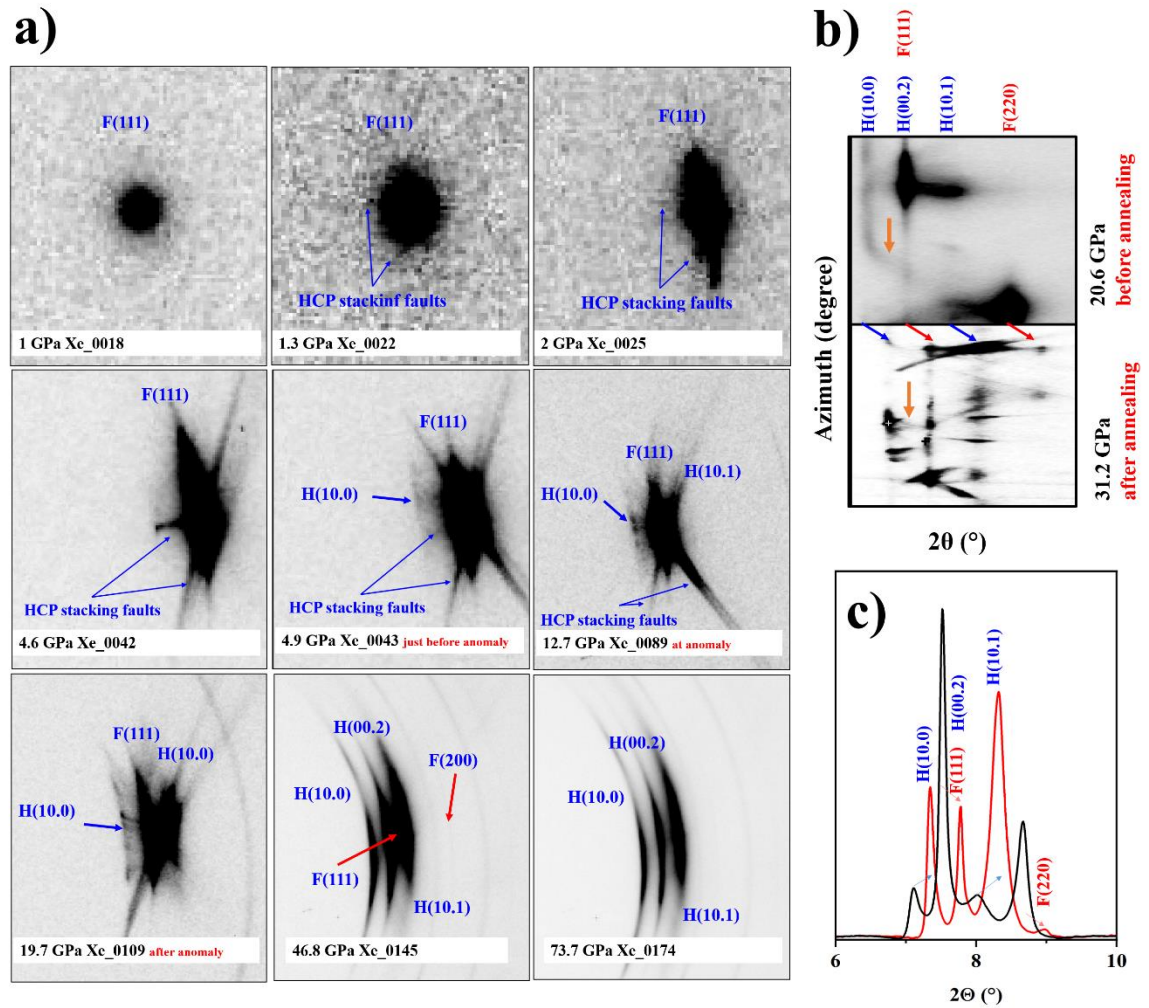
244 As presented in **Table I**, two independent X-ray diffraction (XRD) runs were carried out
245 on solid xenon. Following the same methodology as for krypton [32], run-1 was devoted to the
246 detailed investigation of the fcc to hcp martensitic transformation, the effect of temperature
247 annealing and the determination of the equation of state (EoS) of fcc and hcp xenon, in a wide
248 pressure regime up to 85 GPa. A large number of data points (75 data points) were collected in
249 this run to increase the precision on the determination of the EoS parameters. As it was conducted
250 in a large overlapping pressure interval (~ 40 GPa) with run-1, run-2 was used to control the

251 consistency of the obtained results, increase their precision and robustness and further study the
252 effect of temperature annealing on the fcc-hcp transition.

253 A series of diffraction images from run-1, recorded between 1 and 73.7 GPa, is presented
254 in **Fig. 2**. At 1.09 GPa, a fcc single-crystal is observed. At this pressure, the intensity distribution
255 in the (111) Bragg reflection is homogeneous and no trace of diffuse scattering is observed. At
256 slightly higher pressure ($\Delta P \sim 0.3$ GPa), this diffraction peak largely deforms and a weak diffuse
257 intensity is growing up in its vicinity. A careful analysis of the pressure induced intensity transfer
258 from the fcc to the hcp phase along the [111] direction indicates that the appearance of X-ray
259 diffuse signal is linked to the onset of the fcc/hcp martensitic transition. The presence of X-ray
260 diffuse scattering was reported previously for xenon and krypton [30-32] and related to the
261 presence of an increasing number of stacking faults (SFs) along the fcc [111] direction. For xenon,
262 the onset of the fcc/hcp transition is precisely located at 4.9 GPa. As shown in **Fig. 2**, above this
263 pressure, a progressive splitting of the (111) fcc reflection into the hcp (100), (002) and (101)
264 reflections is recorded on panoramic XRD images. Single-crystal XRD measurements at this
265 pressure confirmed that the martensitic phase transition in xenon produces an hcp phase with the
266 expected orientation relation: fcc (111) // hcp (0001) and fcc [1-11] // hcp [1-210].

267 Similarly to krypton [32] and as shown in **Fig. 2b**), the X-ray diffuse signal present at
268 ambient temperature remains very intense after temperature annealing ($T > 2400$ K) in the entire
269 pressure domain of fcc-hcp phase coexistence. This strongly suggests that the fcc-hcp transition
270 and the presence of hcp SFs are not due to non-homogeneous stress distribution in the pressure
271 cavity. This is also supported by the deviatoric stress analysis of the XRD peak positions of the
272 gold sample in run-1 and run-2 (**Fig. S4 and S5, Supplementary Material**). This analysis reveals
273 quasi-hydrostatic pressure conditions in the sample chamber up to ~ 15 GPa in run-1 and over the

274 entire investigated pressure range in run-2. At pressures above ~15 GPa, a small deviatoric stress
275 of 0.14 GPa develops in run-1 that increases to a moderate value of 0.5 GPa at 71 GPa. For
276 comparison, this value is of the same order as in helium, a quasi-hydrostatic pressure medium [47],
277 although an increase in strength with rare gas weight is expected. Martensitic transitions
278 commonly induce shape changes of a transforming crystal during the collective shuffling of atoms
279 [1]. This shape change can lead to the built up of internal stress in the crystal that is known as
280 transformational stress [1]. The formation of multiple equivalent-sized martensite variants can
281 counterbalance the shape change and limits thus the transformational stress [1,53]. The same
282 mechanism could also release non-hydrostatic stress that is usually build in the diamond anvil cell
283 by thinning of the gasket. The very low deviatoric stress observed in gold above the transition
284 pressure (**Fig. S4** and **S5**) suggests that this mechanism could be at work here.



285

286

287 **Figure 2a) left panels:** Series of diffraction images from run-1 on pure xenon, showing the evolution of the
 288 xenon fcc (111) reflection (denoted as $F(111)$) with increasing pressure, the onset of the X-ray diffuse
 289 scattering linked to the emergence of the hcp phase and hcp Bragg reflections (denoted as $H(10.0)$, $H(00.2)$
 290 and $H(10.1)$) after completion of the phase transition at ~ 74 GPa. **b) and c) right panels:** X-ray diffraction
 291 images (top) and corresponding integrated patterns (down) from run-2 on xenon before and after annealing
 292 at $T = 2400$ K. Note the pressure increase due to temperature annealing.

293

294 3.2 Anomalous compression behavior

295

296 From run-1 and run-2, we have accurately determined the effect of the martensitic
297 transformation on the equation of states (EoS) of fcc and hcp xenon. In particular, we examined
298 the effect of the increasing concentration of stacking faults on these EoS. We have finely explored
299 the low-pressure regime to better constrain the ambient pressure atomic volume (V_0) and examined
300 the effect of temperature annealing. The pressure variation of the atomic volume of fcc and hcp
301 xenon from this study are presented in **Fig. 3** and compared to the literature [30,54,55] in **Fig. S6**
302 **(Supplementary Material)**. The P - V data from run-1 and -2 are in excellent agreement in their
303 overlapping pressure domain for both the fcc and hcp forms. As evidenced in **Fig. 3** and **S6**
304 **(Supplementary Material)**, the present dataset exhibits lower dispersion than the literature ones
305 resulting in a more accurate determination of the equation of state parameters. From the absence
306 of observable deviation of the atomic volume of xenon after high temperature treatment, we also
307 could confirm that, similarly to krypton [31,32], temperature annealing has a negligible effect on
308 the compression behavior of xenon.

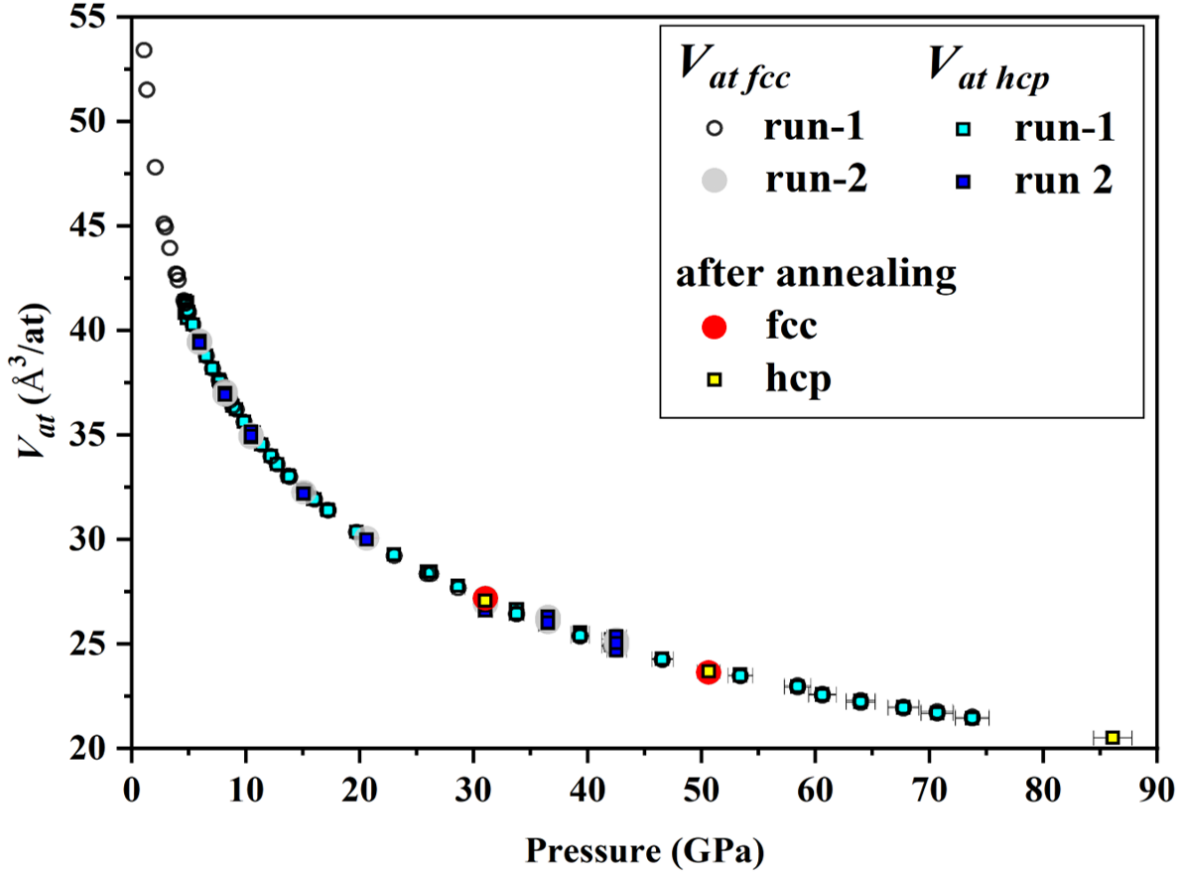


Figure 3. Pressure evolution of the atomic volume V_{at} (\AA^3) for the fcc and hcp phases of xenon. The pressure has been determined using the ruby luminescence technique Dewaele et al. [43] up to 60 GPa beyond this pressure the pressure from the unit cell volume of gold was used and the EoS reported in Dewaele et al. [43]. Uncertainties on V_{at} are in the order of 10^{-3} and smaller than the symbol size. The symbols for the fcc phase of run-2 and after annealing have been enlarged for better visualization but bear the same uncertainties as other points. Note that the effect of temperature annealing on V_{at} is negligible and that there is little difference between V_{at}/fcc and V_{at}/hcp that is below 1% (**Table SI**). The literature data are presented in the left inset panel.

309 The equation of state parameters, *i.e.* the unit-cell volume at ambient pressure V_0 , bulk
310 modulus K_0 and first derivative K' for fcc and hcp xenon were derived by adjusting the P - V data

311 to a Vinet EoS using the software EoSFit [56], taking into account the uncertainties on P and V .
 312 The obtained V_0 , K_0 and K' for fcc and hcp xenon are listed together with literature values in **Table**
 313 **II** and **III**, respectively.

314 **Table II.** Equation of state for fcc xenon: model and fit parameters V_0 , K_0 , K' , pressure range
 315 and number of data points from this work and the literature.

fcc xenon	model	V_0 (\AA^3)	K_0 (GPa)	K'	P range (GPa)
This study	Vinet	235.15(9)	4.54(2)	6.26(1)	1 – 74 GPa (75 points)
Dewaele et al. 2012 [57]	R.-Vinet ¹ (0 K)	233.76	4.887	6.18(5)	4 – 50 (20 points)
Errandonea et al. 2002 [31]	BM ² 3 rd	249.75	4.3(6)	5.7(5)	1.5 – 41 (8 points)
Cynn et al. 2001 [30]	BM ² 3 rd	252.21	3.6(5)	5.5(4)	3-50 GPa (29 points)

316 ¹R.-Vinet - Rose–Vinet
 317 ²BM - Birch-Murnaghan
 318

319 **Table III.** Equation of state for hcp xenon: model and fit parameters V_0 , K_0 , K' , the pressure
 320 range, number of data points from this work and the literature.

Hcp xenon	model	V_0 (\AA^3)	K_0 (GPa)	K'	P range (GPa)
This study	Vinet	118.71	4.24(4)	6.35(3)	4.6 - 86 Gpa (65 points)
Dewaele et al. 2012 [57]	R.-Vinet ¹ (0 K)	114.82	4.887 fixed	6.2955	10 - 260 Gpa
Cynn et al. 2001 [30]	BM ² 3 rd	126.10	4.3(3)	4.9(1)	52-127 Gpa (15 points)

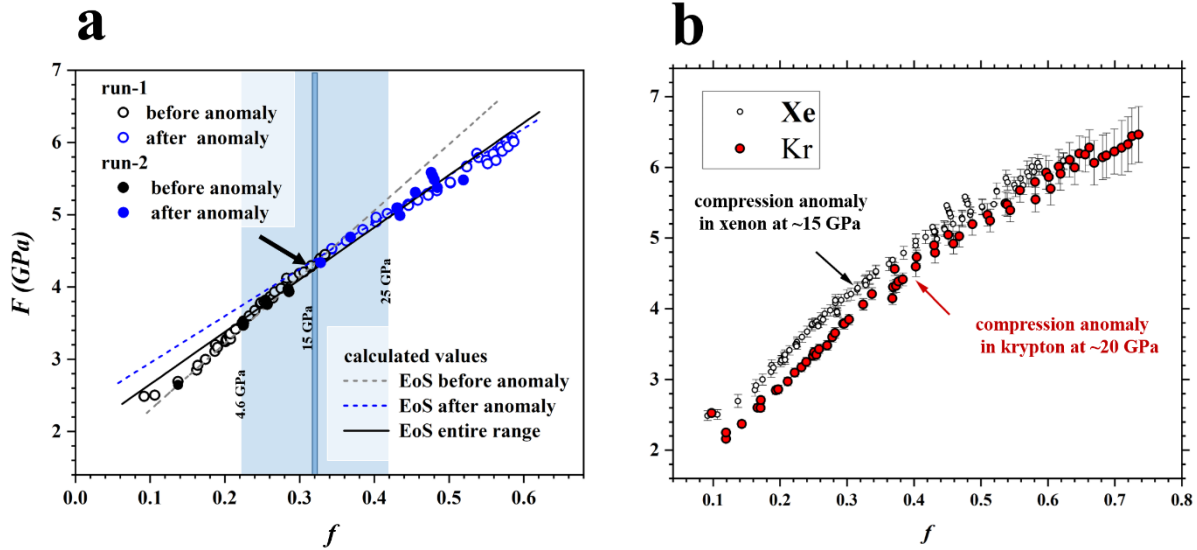
321 ¹R.-Vinet - Rose–Vinet
 322 ²BM - Birch-Murnaghan
 323

324 They are in good agreement with the values of Dewaele et al. [57] but substantially deviate
 325 from the ones reported in reference [30,31]. This could originate from the high number of

326 measured data points (75) in the present work, in particular at low pressure, where a slightly larger
327 data dispersion can induce a large error in V_0 . As for krypton [32], a near ideal c/a ratio for hcp
328 structures ($\sqrt{8/3} = 1.633$) is observed for all the hcp data points (**Table I** and **Fig. S7 top panel,**
329 **Supplementary Material**) attesting a similar reduction of the two crystallographic axis a and c of
330 xenon with increasing pressure. The axial ratios of most hcp metals fall in the range $1.57 < c/a$
331 > 1.65 and show very little variations with pressure as discussed in Kenichi [58]. The near to ideal
332 c/a ratio found for Xe over the probed pressure range of 1.631(2) may rule out the existence of an
333 intermediate orthorhombic close-packed structure as previously proposed [29,59] and may rather
334 indicate a progressive martensitic transformation related to the increasing fraction and thickening
335 of stacking faults in the material. In Kr, Rosa et al. [32] observed a slight deviation from the near
336 ideal c/a ratio especially in the low-pressure regime for which the hcp volume fraction remains
337 below 20% (**Fig. S7 bottom panel, Supplementary Material**). This may suggest a structural
338 distortion of the hcp SFs seeds from the ideal hcp structure.

339 Another source of uncertainty in the determination of the EoS parameters of xenon could
340 arise from the nature of the fcc/hcp martensitic transformation. Indeed, it was shown that krypton
341 exhibits an anomalous compression behavior related to the presence of an increasing number of
342 hcp domains of nano-metric size [32]. This singular behavior was determined from the correlation
343 between the pressure dependence of the volume fraction of the hcp phase and the anomaly in the
344 normalized pressure, F , versus Eulerian strain, f [60,61], where $f = [(V/V_0)^{-2/3} - 1]/2$ and $F =$
345 $P/(3f(1+2f)^{5/2})$. The Ff plot analysis is a standard method to detect compression anomalies that are
346 not obvious in the regular evolution of the compression curve (P - V plot). We have conducted a
347 similar Ff plot analysis for xenon. As shown in **Fig. 4a**, a clear deviation to a linear variation is
348 evidenced in fcc xenon at a pressure of ~ 15 GPa. As already mentioned, such a non-linear effect

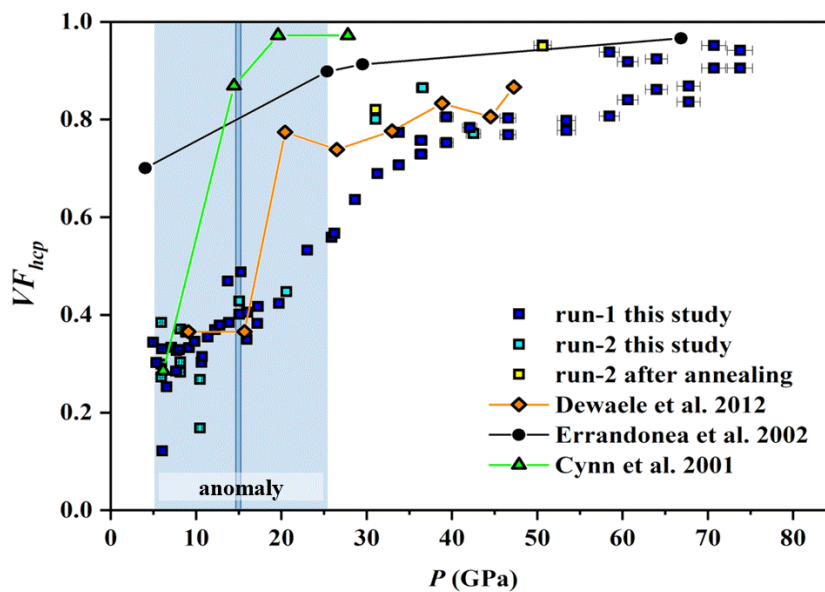
349 has also been determined in solid krypton at slightly higher pressure (~20 GPa) [32] suggesting a
 350 systematic evolution of the underlying microscopic mechanism during the fcc/hcp martensitic
 351 transition in heavy noble solids (**Fig. 4b**).



352
 353 **Figure 4a)** Normalized pressure, F in GPa, vs. Eulerian strain f , for the fcc phase of xenon and **b)**
 354 compared to the one found for krypton in a previous work [32]. The grey and blue dashed lines correspond
 355 to calculated values from fitted EoS using the data obtained before (open symbols) and after (filled symbols)
 356 the anomaly. The black solid line corresponds to the data fitting over the entire P domain (up to 74 GPa).
 357 Uncertainties are 2% for the pressure and are within the symbol size for the Eulerian strain f and F . The
 358 interval of the compression anomaly where a deviation from a linear compression behavior occurs is
 359 highlighted by the light blue shaded area. The turn-over over point of the compression behavior is indicated
 360 with an arrow and a dark blue line in a). It appears for xenon at ~15 GPa and it is derived from the crossing
 361 of the two independent EOS fits, before and after the anomaly. Note that we observed a similar behavior in
 362 krypton [32] as shown in b) where the turn-over in compression behavior is indicated by a red arrow.

363
 364 To correlate the observed Ff plot anomaly with the hcp volume fraction (VF_{hcp}), we have
 365 determined its evolution with pressure using multi-phase Rietveld refinement of the XRD patterns

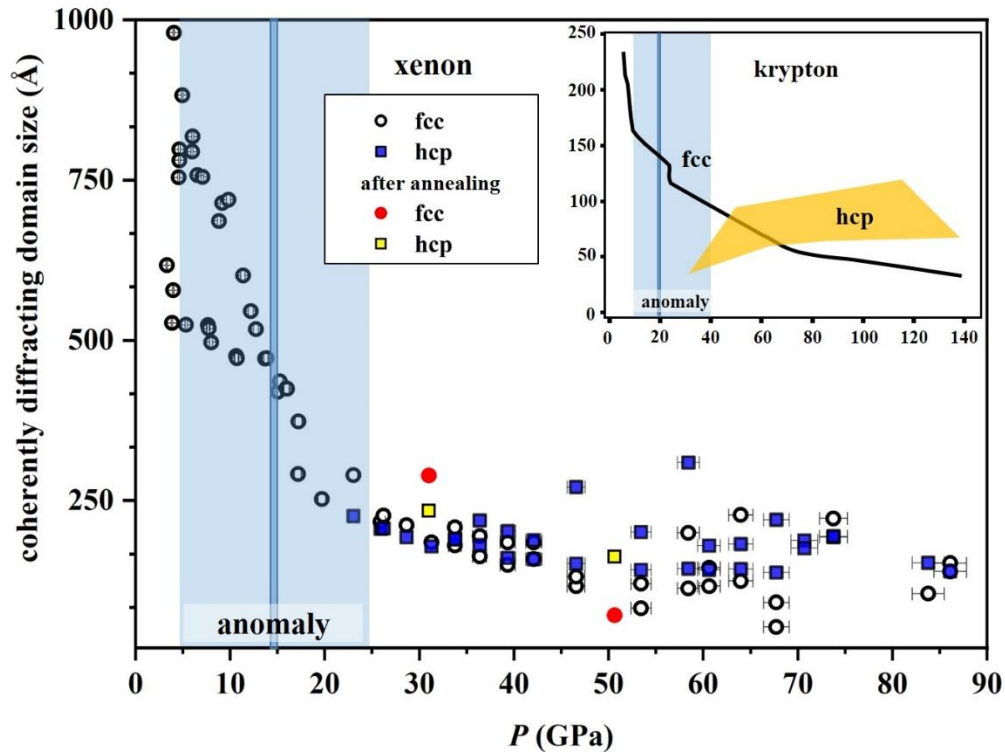
366 using the intensity ratio of all Bragg reflections. As presented in **Fig. 5**, we found a progressive
 367 pressure variation of VF_{hcp} reaching $\sim 100\%$ at ~ 80 GPa. This behavior is contrasting with the one
 368 reported by Cynn *et al.* [30] and Errandonea *et al.* [31] which exhibit a much sharper
 369 transformation. This is maybe related to the differences in the analysis techniques, *i.e.*, Rietveld
 370 refinement (this study) *versus* manual relative peak height analysis (previous works). It is worth
 371 noting that the complete fcc/hcp conversion in xenon occurs at much lower pressure than in
 372 krypton for which the pure hcp phase is expected at ~ 400 GPa. At 15 GPa, the pressure at which
 373 the anomaly in the Ff plot is observed, VF_{hcp} reaches $\sim 40\%$, a value that is twice as large as for
 374 krypton (VF_{hcp} at anomaly $\sim 20\%$). It is also worth noting that the volume fraction VF_{hcp} is not
 375 significantly affected by temperature annealing.



376
 377 **Figure 5.** Pressure evolution of the hcp xenon volume fraction (VF_{hcp}) extracted from Rietveld analysis of
 378 run-1 and run-2 (dark and light blue squares, respectively). Yellow filled squares indicate the data points
 379 obtained after temperature annealing in run-2. VF_{hcp} from the literature obtained by Rietveld refinement of
 380 the intensity ratios of the fcc (200) and fcc (111) + hcp (002) reflections are indicated. Blue bar: pressure

381 *at which the anomalous compression behavior is observed. At this pressure, VF_{hcp} is ~40 %. In this study,*
382 *the uncertainty on VF_{hcp} is of the order of 6% and smaller than the symbol size.*

383 As presented in **Fig. 6**, we have also determined the pressure evolution of the coherently
384 diffracting domain size for fcc (CDS_{fcc}) and hcp (CDS_{hcp}) xenon. These quantities were obtained
385 by adjusting the XRD Bragg reflection profiles using Popa's analytical approximation
386 implemented in the software MAUD [62]. We observe a strong reduction with pressure of CDS_{fcc}
387 while the CDS_{hcp} is not significantly affected. This behavior is similar to the one previously
388 observed for krypton [32]. This suggests a generic transformation mechanism in krypton and
389 xenon at the first stages: the increasing fraction of nano-metric hcp SFs propagates, breaks fcc
390 domains into smaller ones and interconnects gradually through the material at a regular pressure
391 rate. The data suggest that the interconnection of hcp domains starting from ~5 GPa leads to the
392 gradual deviation from a regular compression behavior in fcc xenon (**Fig. 4**). It is worth noting
393 that this pressure coincides with the appearance of the first hcp diffraction peaks (**Fig. 2**). At
394 pressures higher than 15 GPa beyond the inflexion point of the compression anomaly, the CDS of
395 the fcc phase does not reduce further contrary to its volume fraction, while the CDS of the hcp
396 phase increases slightly. These observations are similar to those made on krypton (**inset panel of**
397 **Fig. 6**). This suggests that beyond the compression anomaly a modification in the fcc-hcp
398 transformation mechanism occurs that balances the effect of transformational and compressional
399 stresses.



400

401 **Figure 6.** Pressure dependence of the coherently diffracting domain size (CDS) extracted by Rietveld
 402 analysis using Popa's analytical approximation for the fcc and hcp phases of xenon: circles and blue
 403 squares. The red and yellow symbols indicate the data points obtained after temperature annealing. The
 404 uncertainties on CDS extracted from Rietveld are of the order of 15 Å and smaller than the symbol size.
 405 The blue area highlights the pressure domain of the compression anomaly and the blue bar its inflection
 406 point. The pressure dependence of the CDS for the fcc and hcp krypton as reported in [32] is schematically
 407 represented in the inset panel.

408

409 3.3 XAS study of krypton and xenon

410

411 In addition to XRD, we have carried out extended X-ray absorption fine structure (EXAFS)
 412 experiments to follow the pressure evolution of the local atomic arrangement of krypton and xenon

413 during the martensitic transformation. EXAFS provides accurate structural data of the average
414 local atomic environment that complements the information on the individual phases obtained by
415 XRD. In the present study, high-quality EXAFS data of krypton and xenon were acquired in a
416 diamond anvil cell (**Fig. S2 and S3, Supplementary Material**). For both xenon and krypton, we
417 used the same data analysis procedure to investigate next nearest inter-atomic distances R_i between
418 a central absorbing atom and neighboring atoms and their distributions σ^2_i .

419 Three EXAFS runs were performed (**Table I**). In run-3, we have collected EXAFS data of
420 xenon in an extended pressure domain up to 155 GPa to monitor the structural deviations from the
421 ideal fcc and hcp configurations during and after completion of the martensitic transformation.
422 More data points were collected in run-5 and -6 on krypton to investigate with a higher resolution
423 the martensitic transition in the vicinity of the compression anomaly (**Table I**). These data were
424 also used to compare the inter-atomic potential forces to previously reported ones obtained using
425 Monte-Carlo simulations [63].

426 As outlined in section 2.2, the principal objective of the present EXAFS analysis is to
427 constrain the pressure variation of the average next-nearest neighbour distance (R_l) and its
428 distribution (σ^2_l) in order to extract average local structural properties of the bulk material that
429 contains both the fcc and hcp forms. These average properties may progressively deviate from
430 observations of the individual structural properties of the host fcc phase obtained using XRD due
431 to the growth of hcp SFs with reduced lattice volumes that cannot be distinguished easily using
432 XRD.

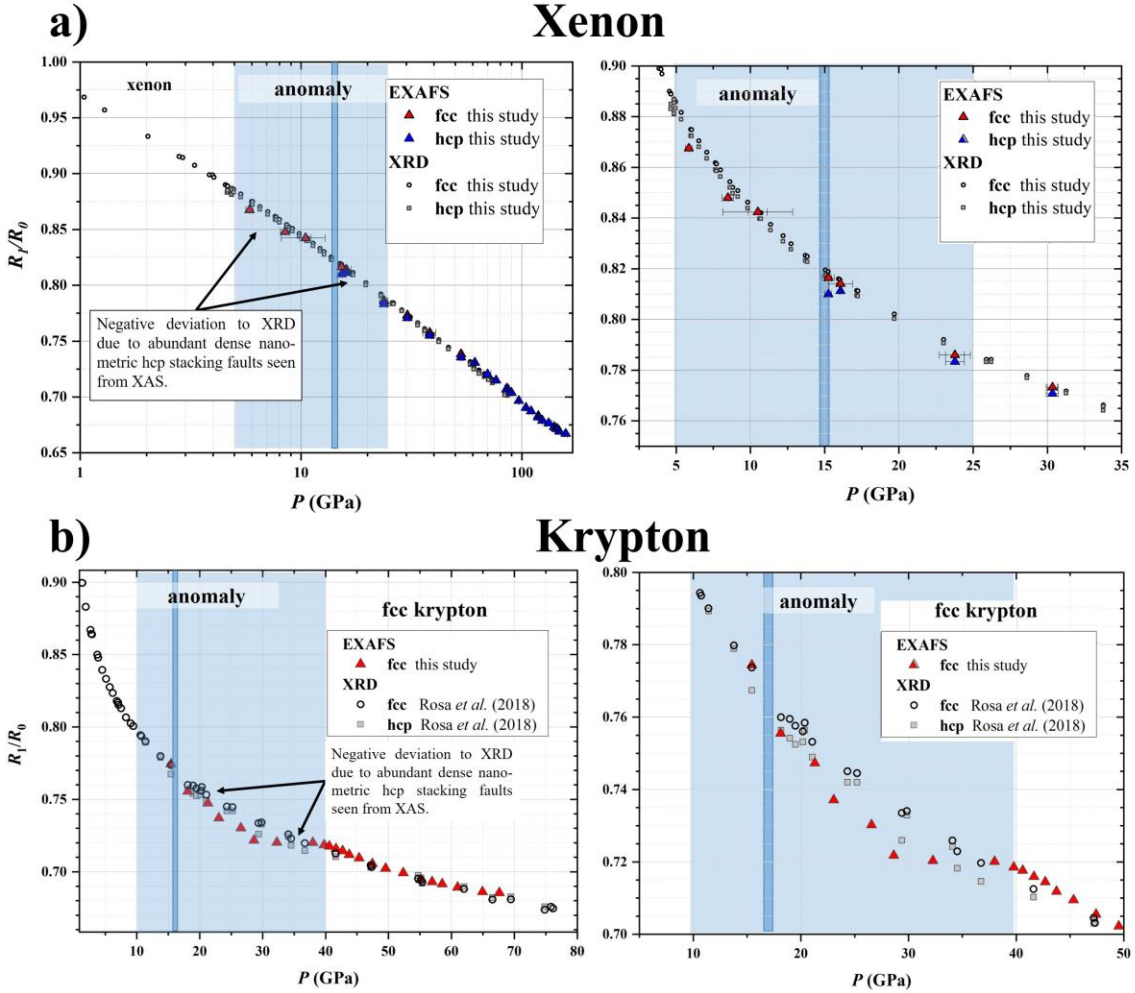
433 As represented in **Fig. 1, S1 and S2**, long-range EXAFS data were acquired up to a k of 16
434 \AA^{-1} providing inter-atomic distances and their distributions up to the third stacking layer of the
435 close-packed planes. Fcc and hcp structures respectively follow an ABCABCABC and

436 ABABABAB pattern types (**Fig. 1** for fcc). The most intense scattering signals of the fcc and hcp
437 forms emerge from paths in the first and second stacking layer. These paths exhibit an equivalent
438 number of next-nearest neighbors and bond distances if the two forms have the same lattice
439 volumes. This complicates the extraction of volumetric fractions and individual lattice volumes
440 from EXAFS fitting, which was therefore not attempted in this analysis. **We used the long-range**
441 **EXAFS data to determine deviations from the ideal fcc and hcp forms seen from XRD by**
442 **extracting the average next-nearest bond distance (R_I) and its distribution (σ^2_I) seen using**
443 **XAS data.** The evolution of average interatomic distances up to the higher stacking layers were
444 also determined (R_2, R_3, R_5) but are only discussed qualitatively in comparisons to R_I as they have
445 higher uncertainties. For clarity, the resulting pressure variations of the extracted bond distances
446 of all scattering paths (R_1, R_2, R_3, R_5 , see **Fig. 1b**) and their distributions are reported in the **Table**
447 **SII and SIII (Supplementary Material)** for xenon and krypton, respectively.

448

449 **3.4 Origin of the compressional anomaly**

450



451

452 **Figure 7a)** Pressure evolution of the first nearest neighbor inter-atomic distances in fcc and hcp xenon
 453 normalized to its value at ambient pressure (R_1/R_0). Data obtained from EXAFS fitting using either the fcc
 454 or the hcp phase as input model are compared to calculated values using the EoS of fcc and hcp xenon
 455 derived from XRD in this study (Table II and III). R_0 was calculated from V_0 as obtained from the EoS of
 456 the present XRD data. A logarithmic pressure scale for xenon data was chosen to highlight the small
 457 deviations between results of different fit models and X-ray probes at low pressures. Uncertainties are
 458 smaller or in the order of the symbol sizes. **b)** Pressure evolution of the first nearest neighbor inter-atomic
 459 distance of fcc krypton normalized to its value at ambient pressure (R_1/R_0). Data obtained from EXAFS
 460 analysis in this work are compared to those acquired from a previous XRD study [32]. R_0 values for fcc
 461 and hcp krypton were calculated from a previous EoS study [32]. The pressure domain of the compressional

462 *anomaly observed in this study in xenon and by Rosa et al. [32] in krypton are highlighted by a blue shaded*
463 *area and the inflexion point of the anomaly is indicated with a blue bar.*

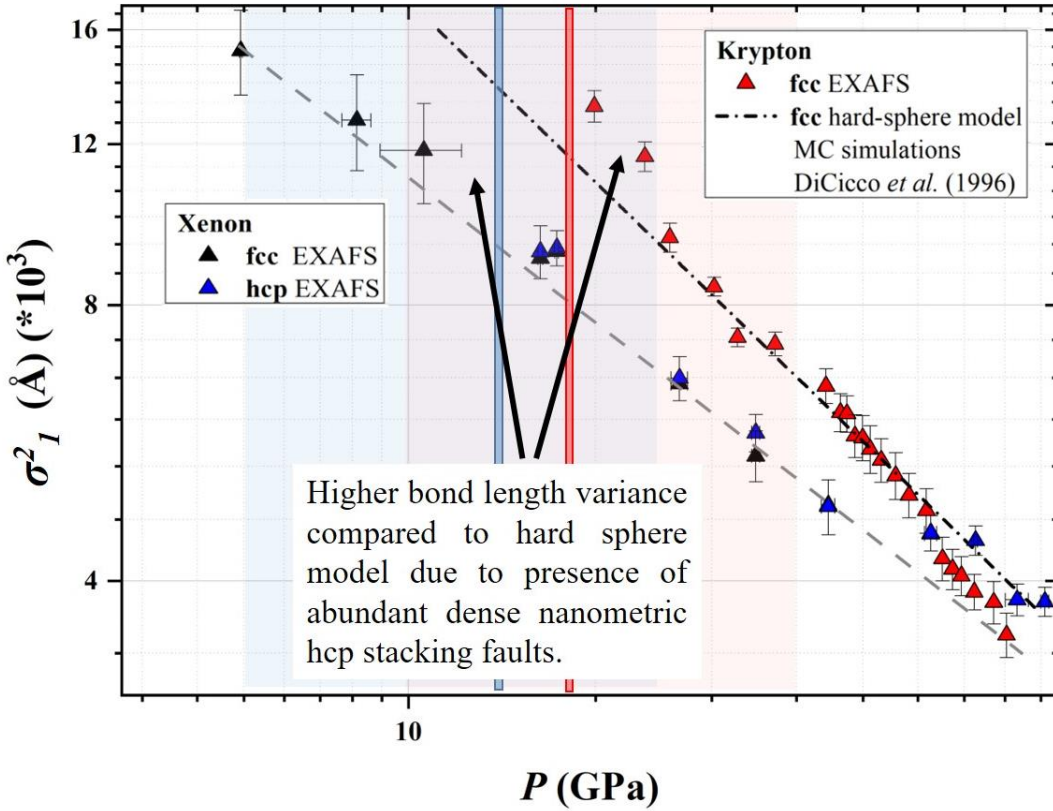
464
465 The evolution of the normalized first nearest neighbor inter-atomic distance R_1/R_0 for fcc
466 and hcp xenon obtained from the EXAFS and XRD analysis are presented in **Fig. 7a**). Above ~25
467 GPa, the results of both X-ray approaches are in good agreement within their mutual uncertainties.
468 Below this pressure, the average first neighbor Xe-Xe inter-atomic distances extracted from the
469 EXAFS data are slightly shorter than those obtained using XRD. However, no definitive
470 conclusion could be drawn from the EXAFS data on xenon regarding the microscopic origin of
471 the compression anomaly due to the few data points sampled in the pressure interval where it
472 occurs (**Fig. 7a**). At pressures above 60 GPa, the first neighbor Xe-Xe distances extracted from
473 EXAFS are slightly larger than those measured by XRD. Such positive deviations were previously
474 related to the existence of anisotropic vibrational modes [51].

475 The larger number of EXAFS data points collected on krypton in run-5 and 6 in the vicinity
476 of the compression anomaly enabled a more detailed interpretation of its origin. As presented in
477 **Fig. 7b**, from the EXAFS data, we observe a strong reduction of the first average neighbor distance
478 (here referred to as Kr-Kr) between ~18 and 36 GPa that is very difficult to assess from the XRD
479 data [32]. We relate this observation to the formation of a large amount of dense hcp SFs in fcc Kr
480 in the pressure interval of the compression anomaly. As it has been demonstrated in our previous
481 XRD data [32], hcp SFs exhibit a shorter next nearest neighbor distances than the parent fcc phase.
482 This observation is supported by the slightly smaller c/a ratio of initial hcp Kr especially in the
483 pressure interval of the anomaly compared to the ideal value ($\sqrt{8/3}=1.633$) (**Fig. S7 bottom, Fig.**
484 **4** in Rosa et al., [32]). Under the assumption that the interatomic distance parallel to the
485 (111)fcc/(0001) hcp plane is unchanged (this assumption is acceptable when the transition

486 proceeds *via* shuffling motion according to Burgers [7]), the c/a ratio directly corresponds to the
487 (111) inter-plane distances. Therefore, the smaller c/a ratio of hcp Kr provide a reasonable support
488 for the shorter interatomic distance measured in the stacking faults. It is worth noting that the
489 inflexion point of the compression anomaly in fcc krypton observed at ~20 GPa from XRD occurs
490 at the onset of the negative deviation of Kr-Kr inter-atomic distances probed by EXAFS. At
491 pressures below or above the compression anomaly, the average Kr-Kr interatomic distances
492 obtained using EXAFS and XRD (for the fcc phase, **Fig. 7b**) are in good agreement. We also note
493 that the c/a ratio extracted from XRD of hcp Kr converges at ~100 GPa (hcp krypton volume
494 fraction of 35%) towards a near ideal c/a value of 1.631 (**Fig. 7b**).

495 A similar conclusion can be qualitatively drawn regarding the pressure evolution of the
496 inter-atomic distances of the 2nd, 3rd and 5th next nearest neighboring atom extracted from EXAFS
497 that deviates from the ideal fcc inter-atomic distances in the region of the compression anomaly
498 for both Xe and Kr (**Fig. S9**). Interestingly, far away from the anomaly at ~60 GPa, the inter-
499 atomic distances in the second and third stacking layer (R_2 , R_3 and R_5) are closer to those of the
500 fcc phase than to those of the hcp phase obtained by XRD (**Fig. S9A**). This suggests the presence
501 of a large fraction of boundary defects between hcp domains that have a local atomic arrangement
502 close to a fcc lattice. Such defects could be located on hcp twins or grain boundaries.

503



504

505 **Figure 8.** Pressure variation of the fitted first neighbor distribution of krypton and xenon (σ^2_1) obtained
 506 from EXAFS. The data are compared to Monte Carlo simulation results using a hard-sphere model
 507 approach [63] for fcc krypton (denoted as MC in the figure legend). A linear trend is expected for a regular
 508 compression behavior. Due to the lack of computational studies for fcc/hcp xenon, we have drawn a linear
 509 line through the data points before and after the compression anomaly as a guide for the eyes.

510

511 As shown in **Fig. 8**, the compression anomaly is also evidenced in the pressure variation
 512 of the first neighbor distance distribution σ^2_1 in krypton and to a lesser extent in xenon. In krypton,
 513 the fitted values of σ^2_1 up to 25 GPa show a strong deviation to the σ^2_1 calculated by Aziz and
 514 Slaman (HFD-B) [64] and reported by DiCicco et al. [63] using a hard sphere model for fcc
 515 krypton. This deviation is reduced but still persistent up to ~ 40 GPa suggesting a high degree of
 516 structural disorder for fcc krypton in the pressure interval of the compression anomaly. A similar

517 behavior occurs for xenon and for the 2nd, 3rd and 5th nearest neighbors in krypton and xenon (**Fig.**
518 **S10, Supplementary Material**). Overall, the pressure dependence of σ^2_I is consistent with the
519 interpretation derived from the evolution of R_i : The increasing fraction of hcp SFs in the fcc
520 structure induces a high degree of structural disorder. This effect is more pronounced in the
521 pressure domain of the compression anomaly because the two structures have differing unit cell
522 volumes at these conditions. Our conclusion is strengthened by our observations beyond the
523 compression anomaly and up to 60 GPa: In this pressure domain we observe a reduction of σ^2_I to
524 the predicted trend of the atomic interaction potential in the hard sphere model of Aziz and Slaman
525 [64]. Beyond 60 GPa, the bond distribution of krypton and xenon deviates from the linear variation
526 expected for a regular compression behavior. In xenon, this behavior could be explained by the
527 presence of a large fraction of boundary defects between hcp domains in the final sample micro-
528 texture close to the completion of the transition.

529 **4. Mechanism of the martensitic transformation**

530 The combined results of EXAFS and XRD suggest a multi-stage growth of hcp SFs in the
531 heavy noble gases krypton and probably in xenon. The proposed microscopic mechanism of the
532 martensitic transformation is presented in **Fig. 9**. Prior to the transformation, the starting material
533 is a high-quality single crystal with well-defined Bragg reflections and without detectable X-ray
534 diffuse scattering that would be the signature of pre-existing defects (**Fig. 2**). In the first stage of
535 the transition (stage 1 of **Fig. 9**), we observe a spontaneous formation of isolated but abundant hcp
536 nano-metric stacking faults along the [111] fcc directions at relatively low pressures (~ 1.3 GPa
537 and ~2.7 GPa for xenon and krypton, respectively). Their growth is evidenced by the presence and
538 increasing intensity of diffuse X-ray scattering signal in the vicinity of the fcc Bragg reflections
539 (**Fig. 2, 5, S8, S11, S12**). Single-crystal XRD analysis (**Fig. S11, S12**) indicates that all possible

540 orientation of hcp domains, with (0001)hcp//(111)fcc (Shoji-Nishiyama orientation relations [1])
541 are observed; this represents four possible orientations, which we call variants here. This is
542 conform to the general concept of the fcc-hcp martensitic transition developed by Olson and Cohen
543 [65] proposing that the first step in martensitic nucleation is characterized by faulting on planes of
544 closest packing resulting from the spontaneous formation of martensitic embryos. A mechanism
545 responsible for the formation of these nano-metric SFs could be the recombination of two Shockley
546 partial dislocations [1], which could generate two twin boundaries in the fcc lattice (**Fig. 9c**). The
547 formation of a large amount of SFs can also explain the significant decrease of CDS_{fcc} (**Fig. 9a**).

548 The second stage of the transition is characterized by the interconnection and thickening
549 of hcp SFs, evidenced by the appearance of distinct hcp diffraction peaks at approximately 15 GPa
550 for Kr [32] and 5 GPa in Xe (**Fig. 2, Fig. S8, S12**). Upon pressure increase, we first observe a
551 rapid and then progressive formation of thin hcp domains which generate more intense XRD peaks
552 (Xe: **Fig. 2, 5, S8, S12 and Kr: Fig. 4** of reference [32]). The formation of a large amount of hcp
553 SFs may explain the strong reduction of the parent phase grain size (**Fig. 6 and Fig 9a**). As
554 evidenced from EXAFS and XRD, in the pressure interval of the compression anomaly the hcp
555 form exhibits shorter next-nearest neighbor distances (up to 4% difference for Kr and 1% for Xe)
556 than the parent fcc phase (Xe and Kr, **Fig. 7**) which may lead to increased local disorder (**Fig. 8**)
557 and to the built up of strain in the material at the fcc-hcp structural boundaries. Based on the
558 compiled observations from EXAFS and XRD (**Fig. 9**), we suggest that the interconnection of
559 dense hcp domains is responsible for the observed compression anomaly in the host fcc phase.
560 This microstructural feature of the transformation is of particular importance as it might be similar
561 to the one responsible for the hardening of metals (*i.e.*, steel hardening). We emphasize that this
562 critical observation can only be made *in situ* and not on quenched materials as the unit cell volumes

563 and local structures are substantially modified during the quenching process. It is also worth noting
564 that the compression behavior of the gold sample located in the pressure cavity is regular over the
565 entire pressure domain (**Fig. S4, S5, Supplementary Material**). This provides additional evidence
566 that the observed compression anomaly in krypton and xenon is intrinsically due to the fcc-hcp
567 lattice mismatch and intergrowth of hcp variants, but not due to the presence of pressure gradients
568 in the sample chamber.

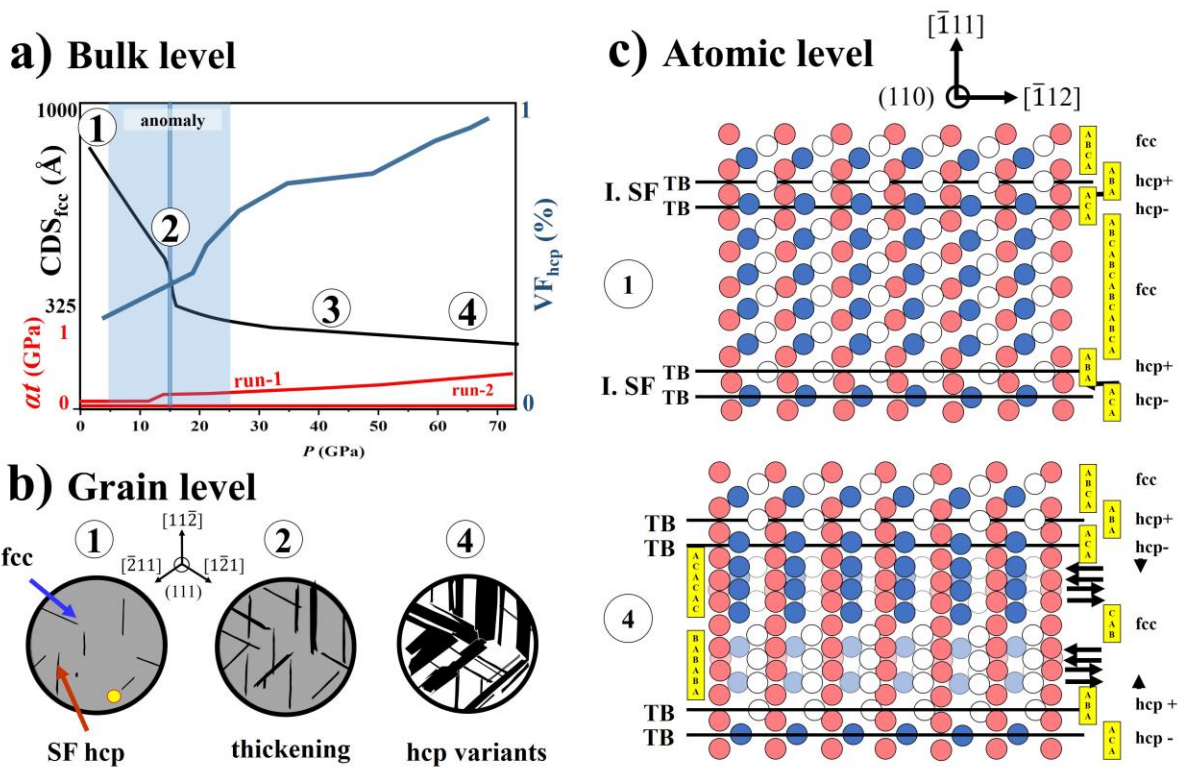
569 Based on total energy considerations, under equilibrium conditions, the densities of
570 coexisting fcc and hcp forms should be similar in the two phases. The observed lower density of
571 the hcp SFs could be related to its nano-metric and defect nature, as well as to the observed slightly
572 smaller c/a ratio compared to the ideal value that suggest a slightly deformed hcp lattice.

573 The third stage of the transformation, after the compression anomaly, is more specific to
574 krypton and xenon. This might be because in steel hardening processes, the quenching of the
575 material would be performed at the stage 2 of the transformation, when the concentration of strain
576 is maximum. At the third stage, the fcc-hcp lattice difference vanishes and the fcc phase retrieves
577 a regular compression behavior (**Fig. 4 and 7, Fig. 9a**). This is also a clear indication that the hcp-
578 fcc lattice mismatch is at the origin of the strain enhancement and compression anomaly. This third
579 stage is characterized by a stagnation of the CDS_{fcc} and CDS_{hcp} and an increase of the hcp volume
580 fraction VF_{hcp} (**Fig. 5, 6 and Fig. 9a**). Based on these microstructural observations, we propose
581 that this third stage might be characterized by the collective shuffling of remaining fcc domains
582 surrounded by hcp SFs. We assume that the formation of new hcp SFs seeds would result in a
583 more drastic reduction of CDS_{fcc} that is not observed beyond the compressional anomaly (**Fig. 6**).
584 Our conclusion is consistent with computational studies that reported a favorable formation of hcp
585 SFs seed in larger fcc domains [34]. The simultaneous growth of equivalent-sized hcp variants due

586 to shuffling of atoms minimize transformational strains [1] and in the present case also reduce non-
 587 hydrostatic stresses naturally present in the DAC at high pressure (Fig. S4, S5, Fig 9a). It was
 588 indeed shown that the formation of coexisting equivalent-sized hcp variants in metals compensates
 589 for the strains induced by the martensitic transition due to crystal shape changes [1,53].

590 Both krypton and xenon preserve the initial strong preferred orientation of the hcp phase
 591 (Fig. 2 and Fig. 1 of reference [32]) up to the maximum investigated pressure. This suggests that
 592 the relative lattice rotations of isolated hcp grains induced by slip systems other than those along
 593 the (111) crystallographic planes play a minor role in the transformation. The proposed
 594 transformation mechanism would result in a final microstructure of the fully transformed material
 595 characterized by a large amount of domain boundaries between hcp variants with fcc-like stacking
 596 sequences as illustrated in Fig. 9c (stage 4).

597



598

599 **Fig. 9.** Evolution of mechanical and microstructural parameters during the martensitic fcc/hcp transition
600 in xenon at **a)** the bulk, **b)** the grain and **c)** the atomic level. The transition is divided in 4 transformational
601 stages: 1) nano-metric Hcp stacking fault (SF) formation from 1.3 GPa onward in xenon, 2) interconnection
602 of SF that induces the compressional anomaly, 3) transformation of remaining fcc domains via shuffling
603 into hcp variant domains of equivalent size and 4) final microstructure of coexisting hcp variants with
604 inverted stacking sequences. In **a)** the pressure dependence of CDS_{fcc} , stress in gold (σ) and VF_{hcp} are
605 summarized. The pressure domain of the compression anomaly is highlighted by a blue shaded area and
606 the inflection point of the anomalous compression behavior is delineated by a blue bar. **b)** summarizes the
607 progression of the transition at the grain scale for the different stages. The yellow circle represents the size
608 of the X-ray beam. At stage 4, hcp variant domains are shown in black and white, to highlight differences
609 in the hcp stacking sequence of either ABABA or ACACA (see **c)** for more details). **c)** Stacking-fault
610 formation and thickening mechanisms at the atomic scale that can explain the observations from both XRD
611 and EXAFS. Note that the stacking sequence of close-packed planes along the $[-111]$ is shown in upward
612 direction. Abbreviations are: TB: twin boundary, I. SF: inverse stacking fault, hcp+ (ABA, stacking
613 sequence) and hcp- (ACACA, stacking sequence).

614

615

616 **5. Conclusion**

617 We have examined the fcc to hcp martensitic transformation in solid krypton and xenon
618 using *in situ* XRD and EXAFS. We have evidenced a multi-stage mechanism in which the
619 transition initially proceeds through the spontaneous nucleation of hcp nanometric domains. This
620 stage is followed by a strain accumulation in the bulk material due to fcc-hcp lattice mismatch and
621 the presence of a large fraction of hcp stacking faults. In this transient domain, an anomaly is
622 evidenced in the equation of state of both materials. In the following stage of the transformation,

623 the lattice mismatch vanishes and a normal compression behavior is retrieved. The micro-texture
624 of xenon in the final stage is characterized by the presence of coexisting hcp variants with inverted
625 stacking sequences. The possible formation of equi-sized hcp variants could explain the low
626 deviatoric stress as seen by the gold pressure marker. The present work reveals the multiple stages
627 of the transformation and disentangles the different effects occurring during the transition. We also
628 provide evidence that the variation of the atomic distances of the parent and martensitic phase
629 during the transformation plays a key role in the building-up and accumulation of strain in the
630 materials' structure.

631 **Acknowledgements**

632 We would like to acknowledge the ESRF for providing beamtime for this work and we are grateful
633 for his help of J. Jacobs during the gas-loading of the samples. We also thank F. Perrin and S.
634 Pasternak for their technical assistance during the experiments. Lawrence Livermore National
635 Laboratory is operated by Lawrence Livermore National Security, LLC, for the U.S. Department
636 of Energy, National Nuclear Security Administration under contract No. DE-AC52-07NA27344.

637 **References**

- 638 [1] Z. Nishiyama, *Martensitic Transformation* (Academic Press New York, 1978), 1st edn.
639 [2] M. Militzer, *A synchrotron look at steel*, *Science* **298**, 975 (2002).
640 [3] D. Fahr, University of California Berkeley,(1969).
641 [4] K. Otsuka and T. Kakeshita, *Science and technology of shape-memory alloys. New developments*,
642 *MRS Bull.* **27**, 91 (2002).
643 [5] B. Ramachandran, P. C. Chang, Y. K. Kuo, C. Chien, and S. K. Wu, *Characteristics of martensitic*
644 *and strain-glass transitions of the Fe-substituted TiNi shape memory alloys probed by transport*
645 *and thermal measurements*, *Sci. Rep.* **7**, 16336 (2017).
646 [6] J. I. Perez-Landazabal, V. Recarte, V. Sanchez-Alarcos, J. J. Beato-Lopez, J. A. Rodriguez-
647 Velamazán, J. Sanchez-Marcos, C. Gomez-Polo, and E. Cesari, *Giant direct and inverse*
648 *magnetocaloric effect linked to the same forward martensitic transformation*, *Sci. Rep.* **7**, 13328
649 (2017).
650 [7] W. G. Burgers, *On the process of transition of the cubic-body-centered modification into the*
651 *hexagonal-close-packed modification of zirconium*, *Phy.* **1**, 561 (1934).

- 652 [8] A. Dewaele, C. Denoual, S. Anzellini, F. Occelli, M. Mezouar, P. Cordier, S. Merkel, M. Veron,
653 and E. Rausch, *Mechanism of the alpha-epsilon phase transformation in iron*, Phys. Rev. B **91**,
654 174105 (2015).
- 655 [9] C. S. Yoo, H. Cynn, P. Söderlind, and V. Iota, *New β (fcc)-Cobalt to 210 GPa*, Phys. Rev. Lett. **84**,
656 4132 (2000).
- 657 [10] R. T. Johnson and R. D. Dragsdorf, *The Martensitic Transformation in Cobalt*, J. Appl. Phys. **38**,
658 618 (1967).
- 659 [11] M. Jiang, K. Oikawa, and T. Ikeshoji, *Molecular-dynamic simulations of martensitic*
660 *transformation of cobalt*, Metallurgical and Materials Transactions A **36**, 2307 (2005).
- 661 [12] T. Komabayashi, Y. Fei, Y. Meng, and V. Prakapenka, *In-situ X-ray diffraction measurements of*
662 *the γ - ϵ transition boundary of iron in an internally-heated diamond anvil cell*, Earth. Planet. Sci.
663 Lett. **282**, 252 (2009).
- 664 [13] F. X. Zhang, S. Zhao, K. Jin, H. Bei, D. Popov, C. Park, J. C. Neuefeind, W. J. Weber, and Y.
665 Zhang, *Pressure-induced fcc to hcp phase transition in Ni-based high entropy solid solution alloys*,
666 Appl. Phys. Lett. **110**, 011902 (2017).
- 667 [14] G. Fiquet, C. Narayana, C. Bellin, A. Shukla, I. Estève, A. L. Ruoff, G. Garbarino, and M.
668 Mezouar, *Structural phase transitions in aluminium above 320 GPa*, C. R. Geosci. **351**, 243
669 (2019).
- 670 [15] Y. Akahama, M. Nishimura, K. Kinoshita, H. Kawamura, and Y. Ohishi, *Evidence of a fcc-hcp*
671 *Transition in Aluminum at Multimegabar Pressure*, Phys. Rev. Lett. **96**, 045505 (2006).
- 672 [16] L. Dubrovinsky, N. Dubrovinskaia, W. A. Crichton, A. S. Mikhaylushkin, S. I. Simak, I. A.
673 Abrikosov, J. S. de Almeida, R. Ahuja, W. Luo, and B. Johansson, *Noblest of All Metals Is*
674 *Structurally Unstable at High Pressure*, Phys. Rev. Lett. **98**, 045503 (2007).
- 675 [17] J. X. Yang, H. L. Zhao, H. R. Gong, M. Song, and Q. Q. Ren, *Proposed mechanism of*
676 *HCP \rightarrow FCC phase transition in titanium through first principles calculation and experiments*,
677 Sci. Rep. **8**, 1992 (2018).
- 678 [18] K. Datta, R. Delhez, P. M. Bronsveld, J. Beyer, H. J. M. Geijselaers, and J. Post, *A low-*
679 *temperature study to examine the role of epsilon-martensite during strain-induced transformations*
680 *in metastable austenitic stainless steels*, Acta Mater. **57**, 3321 (2009).
- 681 [19] A. K. De, J. G. Speer, D. K. Matlock, D. C. Murdock, M. C. Mataya, and R. J. Comstock,
682 *Deformation-induced phase transformation and strain hardening in type 304 austenitic stainless*
683 *steel*, Metall. Mater. Trans. **37a**, 1875 (2006).
- 684 [20] A. I. Tyshchenko, W. Theisen, A. Oppenkowski, S. Siebert, O. N. Razumov, A. P. Skoblik, V. A.
685 Sirosh, Y. N. Petrov, and V. G. Gavriljuk, *Low-temperature martensitic transformation and deep*
686 *cryogenic treatment of a tool steel*, Mat. Sci. Eng. **527**, 7027 (2010).
- 687 [21] U. Dahmen, K. H. Westmacott, P. Pirouz, and R. Chaim, *The Martensitic-Transformation in*
688 *Silicon .2. Crystallographic Analysis*, Acta Metall. Mater. **38**, 323 (1990).
- 689 [22] A. Lai, Z. H. Du, C. L. Gan, and C. A. Schuh, *Shape Memory and Superelastic Ceramics at Small*
690 *Scales*, Science **341**, 1505 (2013).
- 691 [23] G. B. Olson and H. Hartman, *Martensite and Life - Displacive Transformations as Biological*
692 *Processes*, J. Phys. **43**, 855 (1982).
- 693 [24] Y. F. Shen, Y. D. Wang, X. P. Liu, X. Sun, R. L. Peng, S. Y. Zhang, L. Zuo, and P. K. Liaw,
694 *Deformation mechanisms of a 20Mn TWIP steel investigated by in situ neutron diffraction and*
695 *TEM*, Acta Mater. **61**, 6093 (2013).
- 696 [25] R. L. Peng, X. P. Liu, Y. D. Wang, S. Y. Zhang, Y. F. Shen, and S. Johansson, *In-situ Neutron*
697 *Diffraction Study of the Deformation Behaviour of Two High-Manganese Austenitic Steels*, Mater.
698 Sci. Forum **681**, 474 (2011).
- 699 [26] J. Liu and D. Kaoumi, *Use of in-situ TEM to characterize the deformation-induced martensitic*
700 *transformation in 304 stainless steel at cryogenic temperature*, Mater. Charact. **136**, 331 (2018).
- 701 [27] X. S. Yang, S. Sun, X. L. Wu, E. Ma, and T. Y. Zhang, *Dissecting the Mechanism of Martensitic*
702 *Transformation via Atomic-Scale Observations*, Sci. Rep. **4**, 6141 (2014).

- 703 [28] Y. Peng, W. Li, F. Wang, T. Still, A. G. Yodh, and Y. L. Han, *Diffusive and martensitic nucleation*
704 *kinetics in solid-solid transitions of colloidal crystals*, Nat. Commun. **8**, 14978 (2017).
- 705 [29] E. Kim, M. Nicol, H. Cynn, and C. S. Yoo, *Martensitic fcc-to-hcp transformations in solid xenon*
706 *under pressure: a first-principles study*, Phys. Rev. Lett. **96**, 035504 (2006).
- 707 [30] H. Cynn, C. S. Yoo, B. Baer, V. Iota-Herbei, A. K. McMahan, M. Nicol, and S. Carlson,
708 *Martensitic fcc-to-hcp transformation observed in xenon at high pressure*, Phys. Rev. Lett. **86**,
709 4552 (2001).
- 710 [31] D. Errandonea, B. Schwager, R. Boehler, and M. Ross, *Phase behavior of krypton and xenon to 50*
711 *GPa*, Phys. Rev. B **65**, 214110 (2002).
- 712 [32] A. D. Rosa, G. Garbarino, R. Briggs, V. Svitlyk, G. Morard, M. A. Bouhifd, J. Jacobs, T. Irifune,
713 O. Mathon, and S. Pascarelli, *Effect of the fcc-hcp martensitic transition on the equation of state of*
714 *solid krypton up to 140 GPa*, Phys. Rev. B **97**, 094115 (2018).
- 715 [33] P. Schwerdtfeger, N. Gaston, R. P. Krawczyk, R. Tonner, and G. E. Moyano, *Extension of the*
716 *Lennard-Jones potential: Theoretical investigations into rare-gas clusters and crystal lattices of*
717 *He, Ne, Ar, and Kr using many-body interaction expansions*, Phys. Rev. B **73**, 064112 (2006).
- 718 [34] B. Li, G. Qian, A. R. Oganov, S. E. Boulfelfel, and R. Faller, *Mechanism of the fcc-to-hcp phase*
719 *transformation in solid Ar*, J. Chem. Phys. **146**, 214502 (2017).
- 720 [35] S. Pascarelli, O. Mathon, T. Mairs, I. Kantor, G. Agostini, C. Strohm, S. Pasternak, F. Perrin, G.
721 Berruyer, P. Chappellet, C. Clavel, and M. C. Dominguez, *The Time-resolved and Extreme-*
722 *conditions XAS (TEXAS) facility at the European Synchrotron Radiation Facility: the energy-*
723 *dispersive X-ray absorption spectroscopy beamline ID24*, J. Synchrotron Radiat. **23**, 353 (2016).
- 724 [36] O. Mathon, A. Beteva, J. Borrel, D. Bugnazet, S. Gatla, R. Hino, I. Kantor, T. Mairs, M. Munoz, S.
725 Pasternak, F. Perrin, and S. Pascarelli, *The time-resolved and extreme conditions XAS (TEXAS)*
726 *facility at the European Synchrotron Radiation Facility: the general-purpose EXAFS bending-*
727 *magnet beamline BM23*, J. Synchrotron Radiat. **22**, 1548 (2015).
- 728 [37] M. Mezouar, J. P. Perrillat, G. Garbarino, W. A. Crichton, S. Bauchau, and H. Witsch, *Toward*
729 *fully automated high pressure beamlines : Recent developments at beamline ID27, ESRF*, Acta
730 Crystallogr. A **64**, C610 (2008).
- 731 [38] M. Meyer, *Twin samples with CrysAlisPro: Experiments, unit cell finding, data reduction and post*
732 *corrections.*, Acta Crystallogr. A **68**, S83 (2012).
- 733 [39] A. P. Hammersley, *FIT2D: a multi-purpose data reduction, analysis and visualization program*, J.
734 Appl. Crystallogr. **49**, 646 (2016).
- 735 [40] L. Lutterotti, S. Matthies, H. R. Wenk, A. S. Schultz, and J. W. Richardson, *Combined texture and*
736 *structure analysis of deformed limestone from time-of-flight neutron diffraction spectra*, J. Appl.
737 Phys. **81**, 594 (1997).
- 738 [41] See Supplemental Material at [URL will be inserted by publisher] for raw data and detailed
739 analysis results.
- 740 [42] A. Dewaele, A. D. Rosa, and N. Guignot, *Argon-neon binary diagram and ArNe₂ Laves phase*, J.
741 Chem. Phys. **151**, 124708 (2019).
- 742 [43] A. Dewaele, M. Torrent, P. Loubeyre, and M. Mezouar, *Compression curves of transition metals in*
743 *the Mbar range: Experiments and projector augmented-wave calculations*, Phys. Rev. B **78**,
744 104102 (2008).
- 745 [44] A. D. Rosa, M. A. Bouhifd, G. Morard, R. Briggs, G. Garbarino, T. Irifune, O. Mathon, and S.
746 Pascarelli, *Krypton storage capacity of the Earth's lower mantle*, Earth. Planet. Sci. Lett. **532**,
747 116032 (2020).
- 748 [45] A. Dewaele, C. M. Pepin, G. Geneste, and G. Garbarino, *Reaction between nickel or iron and*
749 *xenon under high pressure*, High Pressure Res. **37**, 137 (2017).
- 750 [46] R. Giampaoli, I. Kantor, M. Mezouar, S. Boccato, A. D. Rosa, R. Torchio, G. Garbarino, O.
751 Mathon, and S. Pascarelli, *Measurement of temperature in the laser heated diamond anvil cell:*
752 *comparison between reflective and refractive optics*, High Pressure Res. **38**, 250 (2018).

- 753 [47] K. Takemura and A. Dewaele, *Isothermal equation of state for gold with a He-pressure medium*,
754 Phys. Rev. B **78**, 104119 (2008).
- 755 [48] A. D. Rosa, O. Mathon, R. Torchio, J. Jacobs, S. Pasternak, T. Irifune, and S. Pascarelli, *Nano-*
756 *polycrystalline diamond anvils: key devices for XAS at extreme conditions: their use, scientific*
757 *impact, present status and future needs*, High Pressure Res. **40**, 65 (2019).
- 758 [49] S. Anzellini, A. Dewaele, F. Occelli, P. Loubeyre, and M. Mezouar, *Equation of state of rhenium*
759 *and application for ultra high pressure calibration*, J. Appl. Phys. **115**, 043511 (2014).
- 760 [50] B. Ravel and M. Newville, *ATHENA, ARTEMIS, HEPHAESTUS: data analysis for X-ray*
761 *absorption spectroscopy using IFEFFIT*, J. Synchrotron Radiat. **12**, 537 (2005).
- 762 [51] P. Fornasini, R. Grisenti, T. Irifune, T. Shinmei, O. Mathon, S. Pascarelli, and A. D. Rosa, *Bond*
763 *compressibility and bond Gruneisen parameters of CdTe*, J. Phys.: Condens. Matter **30**, 245402
764 (2018).
- 765 [52] A. Filipponi and A. DiCicco, *X-ray-absorption spectroscopy and n-body distribution functions in*
766 *condensed matter .2. Data analysis and applications*, Phys. Rev. B **52**, 15135 (1995).
- 767 [53] H. Schumann, *Hexagonal Epistolon-Phase in Iron and Iron Alloys*, Arch. Eisenhüttenwes. **40**, 1027
768 (1969).
- 769 [54] D. Errandonea, R. Boehler, S. Japel, M. Mezouar, and L. R. Benedetti, *Structural transformation of*
770 *compressed solid Ar: An x-ray diffraction study to 114 GPa*, Phys. Rev. B **73**, 092106 (2006).
- 771 [55] A. N. Zisman, I. I. Aleksandrov, and S. M. Stishov, *X-ray study of equations of state of solid xenon*
772 *and cesium iodide at pressures up to 55 GPa*, Phys. Rev. B **32**, 484 (1985).
- 773 [56] R. J. Angel, M. Alvaro, R. Miletich, and F. Nestola, *A simple and generalised P-T-V EoS for*
774 *continuous phase transitions, implemented in EoSFit and applied to quartz*, Contrib. Mineral.
775 Petrol. **172**, 29 (2017).
- 776 [57] A. Dewaele, P. Loubeyre, P. Dumas, and M. Mezouar, *Oxygen impurities reduce the metallization*
777 *pressure of xenon*, Phys. Rev. B **86**, 014103 (2012).
- 778 [58] T. Kenichi, *Structural study of Zn and Cd to ultrahigh pressures*, Phys. Rev. B **56**, 5170 (1997).
- 779 [59] A. P. Jephcoat, H.-k. Mao, L. W. Finger, D. E. Cox, R. J. Hemley, and C.-s. Zha, *Pressure-Induced*
780 *Structural Phase-Transitions in Solid Xenon*, Phys. Rev. Lett. **59**, 2670 (1987).
- 781 [60] R. Jeanloz and R. M. Hazen, *Finite-Strain Analysis of Relative Compressibilities - Application to*
782 *the High-Pressure Wadsleyite Phase as an Illustration*, Am. Mineral. **76**, 1765 (1991).
- 783 [61] B. K. Godwal, S. V. Raju, Z. Geballe, and R. Jeanloz, *Electronic phase transitions in cadmium at*
784 *high pressures*, J Phys Conf Ser **377**, 012033 (2012).
- 785 [62] N. C. Popa and D. Balzar, *An analytical approximation for a size-broadened profile given by the*
786 *lognormal and gamma distributions*, J. Appl. Crystallogr. **35**, 338 (2002).
- 787 [63] A. DiCicco, A. Filipponi, J. P. Itie, and A. Polian, *High-pressure EXAFS measurements of solid*
788 *and liquid Kr*, Phys. Rev. B **54**, 9086 (1996).
- 789 [64] R. A. Aziz and M. J. Slaman, *The Argon and Krypton Interatomic Potentials Revisited*, Mol. Phys. **58**, 679 (1986).
- 791 [65] G. B. Olson and M. Cohen, *A general mechanism of martensitic nucleation: Part I. General*
792 *concepts and the FCC \rightarrow HCP transformation*, Metall. Trans. A **7**, 1897 (1976).

793

794 Author Contributions

795 The original idea was conceived by A.D.R. The experiments were performed by A.D.R., G.G., V.S., G.M.,
796 M.K., R.B. and O.M. T.I. provided the nano-polycrystalline diamonds for the X-ray absorption

797 experiments. The data were analysed by A.D.R., A.D., G.G., V.S., F. D. A. and O.M. The manuscript was
798 written by A.D.R and M.A.B with contributions from all the co-authors.

799

800 **Competing Interests statement**

801 The authors declare no competing interests.